UNIVERSITY of York

This is a repository copy of *Tailoring wood waste biochar as a reusable microwave absorbent for pollutant removal:Structure-property-performance relationship and iron-carbon interaction*.

White Rose Research Online URL for this paper:
https://eprints.whiterose.ac.uk/192043/

Version: Accepted Version

Article:
Sun, Yuqing, Zhang, Qiaozhi, Clark, James Hanley orcid.org/0000-0002-5860-2480 et al. (4 more authors) (2022) Tailoring wood waste biochar as a reusable microwave absorbent for pollutant removal:Structure-property-performance relationship and iron-carbon interaction. BIORESOURCE TECHNOLOGY. 127838. ISSN 0960-8524

https://doi.org/10.1016/j.biortech.2022.127838

Reuse
This article is distributed under the terms of the Creative Commons Attribution-NonCommercial-NoDerivs (CC BY-NC-ND) licence. This licence only allows you to download this work and share it with others as long as you credit the authors, but you can't change the article in any way or use it commercially. More information and the full terms of the licence here: https://creativecommons.org/licenses/

Takedown
If you consider content in White Rose Research Online to be in breach of UK law, please notify us by emailing eprints@whiterose.ac.uk including the URL of the record and the reason for the withdrawal request.

White Rose university consortium
Universities of Leeds, Sheffield & York

eprints@whiterose.ac.uk
https://eprints.whiterose.ac.uk/

Tailoring wood waste biochar as a reusable microwave absorbent for pollutant removal: Structure-property-performance relationship and iron-carbon interaction

Yuqing Sun [a,b], Qiaozhi Zhang [b], James H. Clark [d,e], Nigel J.D. Graham [f], Deyi Hou [g], Yong Sik Ok [h], Daniel C.W. Tsang [b,c,*]

[a] School of Agriculture, Sun Yat-sen University, Guangzhou, Guangdong 510275, China

[b] Department of Civil and Environmental Engineering, The Hong Kong Polytechnic University, Hung Hom, Kowloon, Hong Kong, China.

[c] Research Centre for Resources Engineering towards Carbon Neutrality, The Hong Kong Polytechnic University, Hung Hom, Kowloon, Hong Kong, China.

[d] Green Chemistry Centre of Excellence, University of York, York YO105DD, UK

[e] Shanghai Key Laboratory of Atmospheric Particle Pollution and Prevention (LAP3), Department of Environmental Science and Engineering, Fudan University, Shanghai 200438, China.

[f] Department of Civil and Environmental Engineering, Imperial College London, South Kensington Campus, London SW7 2AZ, UK.

[g] School of Environment, Tsinghua University, Beijing 100084, China.

[h] Korea Biochar Research Centre, APRU Sustainable Waste Management Program & Division of Environmental Science and Ecological Engineering, Korea University, Seoul 02841, Korea.

* Corresponding author email: dan.tsang@polyu.edu.hk

Abstract

This study innovated the concept in designing an efficient and reusable microwave (MW) absorbent through concurrent exploitation of carbon graphitization, oxygen functionalization, and carbothermal iron reduction underpinned by an endothermic co-pyrolysis of wood waste and low-dosage iron. A powerful MW assimilation was accomplished from nanoscale amorphous magnetic particles as well as graphitized microporous carbon-iron skeleton in the biochar composites. Relative to a weak magnetic loss derived from the iron phase, the graphitic carbon architecture with abundant surface functionalities (*i.e.*, C−O and C=O) exhibited a strong dielectric loss, which was thus prioritized as major active sites during MW reuse. The MW-absorbing biochar demonstrated a fast, robust, and durable removal of a refractory herbicide (2,4-dichlorophenoxy acetic acid) under mild MW irradiation with zero chemical input, low electricity consumption, and negligible Fe dissolution. Overall, this study will foster carbon-neutral industrial wastewater treatment and wood waste valorization.

Keywords: microwave absorption, engineered biochar, iron-biochar composite, sustainable wastewater treatment, wood waste recycling/management.

1. Introduction

There is an increasing deterioration and scarcity of water resources, caused partly by the ubiquitous distribution of toxic and resistant synthetic organic contaminants (Palansooriya et al., 2020). Future

wastewater treatment should be consistent with the global consensus on low-carbon, sustainable technology featuring energy saving and resource circulation (Kamali et al., 2021). Microwave-assisted wastewater treatment is attractive with a reduced reactor size, short reaction time, limited chemical addition, and low energy consumption (Wei et al., 2020). These advantages are primarily dependent on the design of eco-friendly microwave absorbent. The ideal microwave absorber can effectively convert electromagnetic wave radiation into thermal or other types of energy, to induce thermal activation and generation of oxidative radicals from water molecules for organics degradation (Xia et al., 2022).

Carbonaceous materials with adjustable dielectric properties and iron-based materials with strong magnetic responses are commonly used microwave absorbents (Wang et al., 2018). However, they usually display poor performance due to inferior porous architectures, high density, and easy oxidation/corrosion (Shukla, 2019). Recently, iron-carbon composites derived from high-temperature (> 800 °C) calcination of iron-containing metal-organic frameworks (MOFs) have attracted intensive research interest as effective microwave absorbents (Liu et al., 2021a, 2021b). However, a plethora of fossil fuel-derived energy and chemicals were exhausted during the complicated synthesis procedures (Zhao et al., 2019). In contrast, an iron-biochar composite produced from negative-emission, economical-feasible, scalable, and renewable one-pot pyrolysis of waste forestry biomass, would be a highly advantageous substitute (Kim et al., 2020). This material can benefit from the complementary nature of the carbon and iron compositions for synchronous dielectric loss and magnetic loss to promote microwave absorption capacity.

59 Recent research studies have demonstrated the promising performance of iron-biochar composites as a
60 microwave-active catalyst for organics removal from wastewater. Lv et al. (2019) produced a sludge-derived
61 biochar by means of 650°C pyrolysis and ~20 *wt.*% Fe precipitation. With additional hydrogen peroxide
62 (H_2O_2, 0.3 M), this magnetic biochar composite achieved fast degradation of bisphenol S *via* a Fenton-like
63 reaction and maintained a stable efficiency for three cycles. Cai et al. (2020) prepared an Fe/Fe_3C@C powder
64 through calcinating a mixture of Fe^{3+} and citric acid (molar ratio of 1:2) at 700°C. This catalyst exhibited
65 super-fast removal of methyl orange without extra oxidant. Nevertheless, the composites were synthesized
66 without scientific hypothesis to unravel the structure-property-performance relationships. In particular, the
67 over-loaded Fe content (*e.g.*, > 20%) and use of citric acid dissipates valuable resource/energy and results in
68 low reusability as well as secondary environmental contamination due to substantial Fe leaching. Overall, the
69 available literature is limited in these critical aspects, which would restrict the practical application of
70 microwave-assisted wastewater treatment.
71 This study aims to shed light on the essential microwave-absorbing properties and iron-carbon interactions
72 in producing a tailored biochar composite as an efficient, reusable, and environmentally friendly microwave
73 absorber that can accomplish the rapid removal of a representative refractory organic contaminants with low
74 energy and chemical consumption. The following hypotheses were thus proposed: (i) At different pyrolysis
75 conditions, both biochar and loaded Fe species can evolve from microwave-transparent materials to a
76 microwave-absorbent; the composite characteristics including graphitic carbon, reduced Fe-based magnetic

77 particles, oxygen functional groups, defective structure, and hierarchically porous carbon-iron interfaces,
78 would be closely related to its microwave absorption capacity. (ii) A low dosage of Fe impregnation can
79 catalyze reformation of carbon structure during co-pyrolysis, while a high dosage of Fe would block the
80 porous structure and detach from the biochar matrix.

81 By virtue of multiple advanced spectroscopic analyses, this study disseminated that sufficient MW-assisted
82 organic removal, energy efficiency, and reusability of the composites required high MW absorption ability
83 corresponding to dielectric and magnetic loss, which could be maximized by the formation of nano-sized
84 amorphous magnetic particles, rich defective sites, and abundant surface functionalities on the graphitized
85 microporous carbon-iron skeleton. These composite features were pivotal for the beneficial Fe-catalytic
86 effects on both the carbothermal reduction of Fe speciation and carbon structure evolution during the
87 endothermic reactions. Overall, this study could provide valuable insights into application-oriented design of
88 biochar composites for microwave-assisted wastewater treatment.

89

90 **2. Materials and Methods**

91 ***2.1 Chemicals***

92 All the chemicals used in this study were of analytical grade and solvents were of high-performance liquid
93 chromatography (HPLC) grade. Detailed information can be found in the previous study (Sun et al., 2020).

94 ***2.2 Tailored preparation of biochar composites***

A lignocellulosic waste biomass, namely oak tree sawdust with intrinsic porous structure, high lignin content, and low impurity (Jing et al., 2022), was collected from a furniture manufacturer in Wuxi (Jiangsu Province, China) and used as a precursor material without acid washing. The wood biomass was cut and crushed to pass through a 30-mesh sieve (particle size < 0.6 mm), and then oven-dried at 60 °C overnight before use. An aliquot of the wood powder (10 g) was mixed uniformly with a certain amount of $FeCl_3 \cdot 6H_2O$, giving Fe to biochar mass ratios of approximate 1, 5, and 10% (according to the biochar yield at the selected pyrolytic temperature), respectively, in 600 mL deionized water (DIW) in a ceramic container by a magnetic stirring apparatus at room temperature for 24 h. The liquid-solid mixture was then evaporated in a 105°C oven overnight. To rationally tune the porosity, graphitization level, surface functionality, and Fe speciation of the iron-biochar composites, the solid residue was ground for homogeneity and pyrolyzed in a tube furnace that was heated to four different temperatures (*i.e.*, 500, 700, 800, and 900 °C) at a ramping rate of 10 °C min^{-1}, and held for 2 h at the target temperature with continuous N_2 purging at a flowrate of 200 mL min^{-1} (Xu et al., 2021). After cooling to ambient temperature inside the furnace through a 30-min slow air-N_2 exchange, the stabilized samples were taken out and stored in air-tight containers for further use. The obtained samples were denoted as FeXBCY, where X (X = 1, 5, and 10) and Y (Y = 500, 700, 800, and 900) represented the Fe loading ratio (%) and pyrolytic temperature (°C), respectively. The pristine biochars (denoted as BC500, BC700, BC800, and BC900) were also prepared following the same protocols above.

Detailed information about the microwave absorption ability of biochar composites was comprehensively

characterized. The analyses included vector network analyzer (Agilent, HP8722ES, USA), transmission electron microscopy coupled with energy dispersive X-ray spectroscopy (TEM-EDX) (Thermo Fisher Scientific, FEI Talos F200X, USA), X-ray diffraction (XRD) (Rigaku SmartLab, Japan), N_2 isothermal adsorption-desorption analyzer (Micromeritics, ASAP2460, USA), Micro-Raman spectroscopy (Renishaw, UK), X-ray photoelectron spectroscopy (XPS) (Thermo Fisher Nexsa, USA), Fe *K*-Edge X-ray absorption near-edge structure (XANES) and extended X-ray adsorption fine structure (EXAFS) spectroscopy coupled with linear combination fitting (LCF) and wavelet transformation (WT) analyses, and thermogravimetry-derivative thermogravimetry-differential scanning calorimetry (TG-DTG/DSC) (Netzsch, STA 449F3, Germany). Analytical conditions and detailed procedures can be found in the previous studies (Feng et al., 2020; Lin et al., 2007; Sun et al., 2019, 2020).

2.3 Microwave-assisted removal of organic contaminant

As one of the most widely used herbicides and possible human carcinogens, the ubiquitously detected and easily mobilized organic contaminant, 2,4-dichlorophenoxy acetic acid (2,4-D), with a high water solubility (900 mg L^{-1}), recalcitrant chemical structure, low biodegradability, and moderate toxicity, was selected as a target refractory organic contaminant (Zuanazzi et al., 2020). To initiate the reaction, 20 mg (1 g L^{-1}) of the BC or FeBC composites were transferred into 100 mL Teflon reaction vessels containing 20 mL solution of 2,4-D at an initial concentration of 100 mg L^{-1} (a typical concentration reported in 2,4-D manufacturing wastewaters) without pH adjustment (Sun et al., 2020). The vessels were heated in a microwave (MW) reactor

(Milestone Ethos Up, Italy, 2450 MHz, maximum power of 1500 W). The reactor temperature was ramped from ambient to 90 °C within 2 min, held for 1min, and gradually cooled down to 60 °C by mechanical ventilation in the MW reactor. Constant magnetic stirring was only deployed during the temperature-holding stage, where 2,4-D was in full contact with biochar. The adopted BC/FeBC loading, reaction temperature, and duration, were comparable to previous studies on MW-assisted organic removal (Cai et al., 2020; Lv et al., 2019). After reaction, the liquid phase was filtered using a 0.45-μm mixed cellulose ester (MCE) membrane filter before measurement of 2,4-D concentration and Fe leaching. A control experiment with only MW and no BC or FeBC was also conducted. The 2,4-D adsorption by BC and FeBC was investigated at room temperature (RT) with end-over-end rotation at 50 rpm. After reaction under both MW and RT conditions, the spent samples were collected after vacuum filtration, DIW rinsing, and 60°C oven-dry overnight, and then tested for 2,4-D affinity (by solvent extraction) and reusability. The scavenger tests were implemented under both MW and RT conditions to determine *in-situ* formation of oxidative radicals. All experimental procedures were conducted at least in triplicate, and data were presented as mean values ± standard errors. Detailed information on experimental procedures and analytical parameters is available in the previous study (Sun et al., 2020).

3. Results and Discussion

3.1 Fast 2,4-D removal by the energy-efficient FeBC/MW system

149 The 2,4-D removal was found to depend on both the pyrolytic temperature and Fe impregnation ratio as
150 depicted in **Fig. 1a** (**and see Supplementary Material**). The 900°C-composites displayed clearly greater
151 2,4-D adsorption capacities (47.6−49.3% 2,4-D removal in 1 min) than those prepared at lower temperatures
152 (*i.e.*, 500, 700, and 800 °C), except for a comparably low efficacy (12.0%) of the Fe10BC900. This divergence
153 might be attributed to their larger external surface area, higher graphitization level, and more oxygen-
154 containing functional groups for improved 2,4-D removal *via* pore filling, π-π interactions, and chemisorption
155 (Wu et al., 2021). MW irradiation notably promoted the performances (increase of 11.9−28.2% and
156 25.3−37.7%, respectively) of the high-temperature (*i.e.*, 800 and 900 °C) composites. In contrast, the MW-
157 stemmed improvement was indiscernible for the other composites (**see Supplementary Material**). The low
158 Fe dosages (*i.e.*, 1 and 5 *wt.*%) endowed an upward momentum, albeit with a small rise below 18.0%, in the
159 composite performance under the MW condition. However, the highest Fe loading (*i.e.*, 10 *wt.*%) elicited an
160 opposite impact on those composites. The Fe10BC800 was superior (59.9% *vs.* 16.5−34.5%) whereas the
161 Fe10BC900 was inferior (27.7% *vs.* 74.6−85.4%) than their counterparts, respectively. The critical structure-
162 property-performance relationships of these composites will be comprehensively scrutinized in the following
163 sections.
164 After reaction under the MW condition, even an intensive solvent extraction by methanol was incapable
165 and accomplished less than 33.1% desorption of 2,4-D from the composites (**Fig. 1b**). The particularly high
166 2,4-D affinity (*i.e.*, only 1.8−7.5% 2,4-D desorption) in the Fe10BC800, Fe1BC900, and Fe5BC900 might

167 rely on their abundant microporous structure, graphitized carbon domain, and rich O-functionality (Orduz et
168 al., 2021). This strong bonding unfortunately allowed no procuration of possible degradation intermediates in
169 this study. Nevertheless, the significantly curbed MW-assisted 2,4-D removal (**see Supplementary Material**)
170 by the composites in the presence of various organic scavengers (TBA, FFA, and AA), contrasting the almost
171 unaffected performance under room temperature condition (data not shown), provided a corollary to the *in-*
172 *situ* formation of oxidative radicals ($^{\bullet}OH$, $^{1}O_2$, and $O_2^{\bullet-}$) under MW irradiation for 2,4-D degradation. A more
173 comprehensive experimental-computational design (*e.g.*, full identification of 2,4-D intermediates by mass
174 spectrometry, detection of released Cl^- in the solution, and comparison of different organic contaminants
175 displaying variable interactions with engineered biochar) will further validate and quantify the organics
176 degradation in the MW/Fe-biochar system in future studies.

177 Good energy efficiencies of the prepared FeBC composites (**Fig. 1c and see Supplementary Material**)
178 further demonstrated their versatility in developing the MW-assisted wastewater treatment. Notably, the MW
179 reactors containing the BC900, Fe1BC900, and Fe5BC900 showed multifaceted performance ameliorations
180 in 2,4-D removal (74.6−85.4%) as well as electricity consumption (0.014−0.018 kWh/mg 2,4-D). Meanwhile,
181 with an appreciable increase of the reactor temperature (0.4−0.7 °C), these composites intrigued a more
182 efficient MW-to-thermal energy transformation outperforming the conventional thermal activation (Qu et al.,
183 2022). The previous study carried out a comparative study under oil-bath heating with the same experimental
184 setup, which showed that biochar entrapped less 2,4-D even with a much longer (1 min *vs.* 30 min) reaction

time, probably owing to a non-thermal (*i.e.*, "hot-spot") effect on the biochar surface (Sun et al., 2020).

These results unequivocally indicated that this chemical-free and energy-saving FeBC/MW system would be more feasible and sustainable for treating wastewater contaminated with refractory organic herbicides than other types of advanced oxidation processes (AOPs). For instance, the previous reports included photocatalysis (*e.g.*, 92.9% removal of 1.73 mg L^{-1} chlorotoluron in 10 min with 0.060 kWh/mg using ultraviolet radiation and 0.0253 g L^{-1} persulfate as oxidant) (Lai et al., 2022), electrolysis (*e.g.*, 100% removal of 40 mg L^{-1} diuron in 75 min with 0.0962 kWh/mg using the three-dimensional carbon felt/β-PbO_2 anode and 6.1 g L^{-1} Na_2SO_4 as electrolyte) (Rahmani et al., 2021), and ozonation (*e.g.*, 51% removal of 200 μg L^{-1} atrazine in 30 min with 0.160 kWh/mg by purging an ozone/oxygen gas mixture) (Liu et al., 2021c). Moreover, the variable MW performances of the composites strongly depend on their MW absorption capacities, which will be further elaborated in the following sections.

3.2 Roles of the iron and carbon phases in achieving high MW absorption

The 2D projection of MW reflection loss (RL, **Fig. 2a**) illustrated that each composite possessed an optimized MW absorption value (RL_{min}) over the frequency (f_m) range of 2−18 GHz and the thickness (d_m) range of 1−6 mm. The frequency range with an RL value below -10 dB is commonly defined as the effective absorption bandwidth (EAB) where more than 90% of electromagnetic waves can be absorbed (Cao et al., 2019). The Fe5BC900 displayed the smallest RL_{min} (-50.6 *vs.* -27.1−-46.8 dB) and a wide EAB (2.40 *vs.*

1.76−3.68 GHz) at f_m = 11.20 GHz with a thin d_m (2.8 *vs.* 2.7−5.5 mm) compared with the other composites (**Fig. 2b**). Thus, the Fe5BC900 (with only 4.64 *wt.*% Fe) had the strongest microwave absorption capacity, which could even be comparable with the magnetic nano-porous carbon nanorods prepared from the high-temperature calcination of the Fe-based MOF (40 *wt.*% Fe, RL_{min} = -52.9 dB, EAB = 4.56 GHz, d_m = 3.5 mm) (Wu et al., 2019). In this study, the MW absorption capacity of the biochar composites demonstrated a decreasing trend, as follows: Fe5BC900 > Fe1BC900 > BC900 > Fe10BC800 > Fe10BC900 > Fe1BC800 > Fe5BC800 > BC800. This trend is similar to the variations in their MW-assisted 2,4-D removal, energy efficiency, and reactor temperature.

The integral MW absorption capacity of the composite was closely related to the dielectric loss and magnetic loss (tan δ_E and tan δ_M, **Fig. 2c**) derived from the carbon and iron compositions, respectively. For the FeBC900s, the f_m values matching their RL_{min} were shifted to a higher range (8.64−11.20 GHz, where tan δ_M > tan δ_E) than the BC900 (5.76 GHz, where tan δ_M < tan δ_E), implying that the Fe phase was the major MW absorbent. In contrast, the carbon phase largely contributed to MW absorption for the BC800, Fe1BC800, and Fe5BC800, displaying similar f_m values (5.04−5.36 GHz, where tan δ_M < tan δ_E). Interestingly, the Fe10BC800 demonstrated approximately equal values (0.17 and 0.24) of tan δ_M and tan δ_E (at f_m = 7.12 GHz), suggesting both the Fe and carbon phases played essential roles in its MW absorption capacity.

In general, dielectric loss depends on conduction loss and polarization loss (Liu et al., 2021a), while magnetic loss is mainly determined by natural ferromagnetic resonance (Zeng et al., 2020). The following

221 conjectures were raised: (i) graphitic carbon and nanoscale reduced magnetic particles facilitate electron
222 transport to induce conduction loss; (ii) oxygen-functionality and defective structure combined with the
223 graphitic carbon framework accumulate bound charges to produce dipolar polarization; and (iii) hierarchically
224 porous carbon-iron interfaces with uneven charge distribution promote interfacial polarization. These
225 assumptions were then further verified through detailed characterization of the biochar composites.
226
227 ***3.3 Iron induces contrasting catalytic effects on pyrolytic carbon evolution***
228 After the designed fabrication for testing our hypothesis, FeBC composites with distinguishable surface
229 morphologies yet similar Fe compositions were obtained according to the TEM images with EDX mapping
230 and XRD patterns (**see Supplementary Material**). The FeBC800s presented a large amount of nano-sized
231 (32.9−154 nm) iron-oxide particles with high crystallinity (light spots in the SAED patterns) (Nadejde et al.,
232 2015) on the amorphous carbon domain. In contrast, the FeBC composites prepared at 900 °C illustrated that
233 relatively sparse nanoscale (35.4−166 nm) iron-based particles in amorphous form (ring structure without
234 light spots in the SAED patterns) (Nadejde et al., 2015) were encapsulated in the graphitized carbon
235 (crystalline spacing d ≈ 0.250 nm) matrix (Wan et al., 2020). The Fe speciation in all the composites consisted
236 predominantly of magnetite (Fe_3O_4, PDF 89-0688), as indicated by the representative peaks in the XRD
237 patterns and calculated d (~0.279 nm) (Fei et al., 1999) in the HRTEM images. The high Fe loading ratio (*i.e.*,
238 10 *wt.*%) resulted in severe particle aggregation, as evidenced by the largest average crystal size (determined

239 by Scherrer Equation) identified in the Fe10BC800 and Fe10BC900.

240 Obvious variations in the composite surface area and porosity were manifested in **Fig. 3a**. In contrast to the
241 gradually collapsed porous structure in the pristine biochars prepared over 700 °C, more micropores (S_{micro}
242 and V_{micro} increased by 2.56−5.34 and 1.69−3.28 times, respectively) were formed after co-pyrolysis with
243 lower dosages (1 and 5 *wt.*%) of Fe at 900 °C. In comparison, more macro/meso-pores (S_{ext} and V_{total}
244 amplified by 59.4−83.0 and 24.3−30.7%, respectively) were generated under 800 °C. These observations
245 were consistent with the previous findings that metal chlorides (*e.g.*, $CuCl_2$) acted as a pore-forming agent of
246 biochar during high-temperature pyrolysis (Wan et al., 2019). By contrast, thermal treatment at lower
247 temperatures (500 and 700 °C) or with over-loaded (10 *wt.*%) Fe led to blockage of the porous structure in
248 the biochars. The underdeveloped porosity might be a cardinally prejudicial factor in the undifferentiated and
249 mediocre 2,4-D adsorption by these above-mentioned composites (**Fig. 1 and see Supplementary Material**).

250 The different pyrolytic conditions exerted cynosural influences on the graphitization level and interfacial
251 chemical behaviour of the FeBC composites, based on quantitative deconvolution of the Raman (**Fig. 3b**) and
252 XPS (**Fig. 3c and see Supplementary Material**) spectra. With temperature increasing from 800 to 900 °C,
253 no obvious changes in the carbon structure were observed for the pristine biochars (*i.e.*, BC800 and BC900).
254 However, co-pyrolysis with Fe promoted beneficial carbon evolution within this temperature range. The
255 aromatic oxygen-functionality (S) and methylene semicircle ring structures (V_L) in the FeBC800s
256 transformed into defective large aromatic carbon structures (D) and highly ordered sp^2-hybridized graphitic

257 crystallites (G) (Sun et al., 2020; Wan et al., 2019) in the FeBC900s (**Fig. 3b**). Compared with the 800°C-
258 composites (A_D/A_G = 0.43−0.87, $A_D/A_{(VR+VL)}$ = 0.33−0.42), the FeBC900s displayed higher levels of defect
259 (A_D/A_G = 1.00−1.09) and graphitization ($A_D/A_{(VR+VL)}$ = 1.13−1.23) (Wan et al., 2020).
260 Surprisingly, Fe loading results in deterioration of the carbon structure during the 800°C-pyrolysis. With
261 low-dosage (1 and 5 *wt.*%) of Fe, about 50% D band and 30% G band in the BC800 were decomposed into
262 V_L and S bands (**Fig. 3b and see Supplementary Material**). The resultant FeBC composites (*i.e.*, Fe1BC800
263 and Fe5BC800) are inferior in terms of defect level (A_D/A_G = 0.85−0.87 *vs.* 1.12) and graphitization degree
264 ($A_D/A_{(VR+VL)}$ = 0.37−0.42 *vs.* 1.21, π−π transition ratios of 3.32−5.13% *vs.* 11.1%) than the BC800. A similar
265 disrupted carbon structure was observed in the FeBC700s relative to the FeBC500s. A further increased Fe
266 loading (*i.e.*, 10 *wt.*%) completely eradicated the V_L band, and newly formed amorphous carbon structures
267 (V_R) and G band in the Fe10BC800, with a slightly more graphitized carbon domain detected in the HRTEM
268 purview.
269 Moreover, after pyrolysis at 800 and 900 °C, Fe impregnation contributed to more abundant oxygen-
270 functionalities in the composite surfaces (**Fig. 3c and see Supplementary Material**). The ratios of C−O and
271 C=O increased by 5.60% and 7.80% in the Fe1BC900 and Fe10BC900, respectively, in comparison with the
272 BC900. The FeBC800s were also more enriched (11.5−18.4% *vs.* 8.27%) with C=O functional groups than
273 the BC800. Contrastingly, Fe addition at lower temperatures (*i.e.*, 500 and 700 °C) largely consumed the C−O
274 and HO−C=O bonds in the biochars. Thus, this study underscored the importance of catalytic Fe co-pyrolysis

275 in reinforcing oxygen-containing groups (*i.e.*, C=O and C−O) on the biochar surface at high temperatures,
276 which was overlooked in other relevant recurrences (Sun et al., 2019; Xu et al., 2022).
277 It is important to note that Fe impregnation induced intensive carbon evolution but imposed opposite
278 catalytic effects during co-pyrolysis at high temperatures of 800 and 900 °C, respectively. In contrast to the
279 pristine biochars, the Fe1BC900 and Fe5BC900 exhibited a hierarchically microporous skeleton, abundant
280 nano-sized amorphous magnetic particles, a promoted defect level, an enhanced graphitization degree, and a
281 rich O-functionality. These merits were essential for their associated MW-assisted 2,4-D removal due to the
282 synchronously strong 2,4-D adsorption and MW absorption. However, the Fe1BC800 and Fe5BC800
283 demonstrated inferior performances, possibly ascribed to the annihilated carbon structure. In particular, the
284 lowest defect as well as graphitization level ($A_D/A_G = 0.85$, $A_D/A_{(VR+VL)} = 0.37$, **see Supplementary Material**)
285 of the Fe5BC800 were pertinent to its relatively weak MW absorption and poor 2,4-D removal (**Fig. 1**). The
286 excessive Fe (*i.e.*, 10 *wt.*%) alleviated the thermal impact at 800 or 900 °C, probably due to reforming the
287 primeval disordered carbon matrix or blocking the original graphitic porous carbon architecture, respectively.
288 The distinctive physicochemical properties, surface morphology, porous structure, and interfacial chemical
289 interactions were attributed to the iron-carbon interactions during the pyrolytic process.
290
291 ***3.4 Concurrent exploitation of carbothermal reduction of iron and catalytic reformation of carbon***
292 LCF/WT analyses of the XANES and EXAFS spectra (**Fig. 4 and see Supplementary Material**) were

293 further conducted to scrutinize the Fe atoms in the FeBC composites. The LCF results (**Fig. 4a&c**) revealed
294 that magnetite (Fe_3O_4, PDF 89-0688) was the major (50.9−68.0%) Fe component. The WT analysis (**Fig. 4b**)
295 showed similar first and second shell contributions for all the FeBC composites, where the weak/strong back-
296 scattering signals appeared in the energy range of 4−6 and 5−8 $Å^{-1}$, respectively, in accordance with the Fe−O
297 and Fe−Fe scattering of magnetite (Giannetta et al., 2020; Karlsson et al., 2008). The bond distances (**Fig. 4d**)
298 found in the first Fe−O shell (2.00−2.09 Å) and second Fe−Fe shell (2.94−3.10/3.43−3.51 Å) of the samples
299 were in fair agreement with the Fe−O and Fe−Fe bond length reported for magnetite (Changela et al., 2012).
300 Moreover, much lower fractions (19.2−26.7 and 12.8−22.4%) of wustite (FeO, PDF 74-1886) and metallic
301 Fe (Fe^0, PDF 88-2324) were also observed in the composites, consistent with the small representative peaks
302 in the XRD patterns and the calculated crystalline spacing (~0.433 nm of FeO) (Jette and Foote, 1933) in the
303 HRTEM images (**see Supplementary Material**).
304 It was evident that the 800°C-pyrolysis caused the reductive transformation of the Fe species, as the
305 contents of Fe^0 (from 12.8 to 22.4%) and FeO (from 19.2 to 26.7%) were increased with the higher Fe loading
306 ratios (1−10 *wt.*%) in the FeBC800s (**Fig. 4c**). In contrast, the FeBC900s maintained relatively constant Fe
307 composition (*i.e.*, 17.9−19.3% Fe^0, 22.9−24.0% FeO, and 56.7−59.2% Fe_3O_4) irrespective of the Fe dosages.
308 Furthermore, the smallest bond distance (2.94 *vs.* 3.02−3.20 Å) for the short Fe−Fe path in the Fe10BC800
309 implied a major aggregation of iron oxide particles on the biochar composites, which was consistent with the
310 analyses of average crystal size (**see Supplementary Material**) and surface area (**Fig. 3a**). Compared with

311 the Fe1BC900, the Fe10BC900 exhibited a more extended Fe−Fe path (3.49/3.51 *vs.* 3.04/3.43 Å) but a more
312 compact Fe−O path (2.02 *vs.* 2.09 Å), which indicated that the Fe atoms were inserted into the carbon
313 framework, probably *via* Fe−O−C bonding (Sun et al., 2019).
314 The above discussion is further substantiated by evaluating the variations in weight loss and heat flow
315 direction associated with thermal pyrolysis of the Fe-oak mixtures based on the TG/DTG/DSC analyses (**Fig.**
316 **5**). For the oak biomass without the co-existing Fe, char was formed at ~360 °C (line 4 in **Fig. 5b**). The
317 exothermic (*i.e.*, decomposition) or endothermic (*i.e.*, carbonization) reaction occurred below or above this
318 temperature (line 4 in **Fig. 5c**) (Li et al., 2021), respectively. The Fe-induced catalytic effect obviously lowered
319 the required temperature for char formation (Beliy and Udoratina, 2014) to approximately 350, 320, and
320 270 °C (lines 1−3 in **Fig. 5b**) with increasing Fe doses of 1, 5, and 10 *wt.*%, respectively. At lower Fe dosages
321 of 1 and 5 *wt.*%, a tangible mass decay with an upward peak similar with the pristine biomass (lines 5 & 6 in
322 **Fig. 5b&c**) appeared at approximate 631 and 596 °C. This phenomenon might refer to the catalytic char
323 cracking due to depolymerization and fragmentation (Rangabhashiyam and Balasubramanian, 2019), which
324 coincided with the disrupted carbon structure in the FeBC700s rather than FeBC500s. Meanwhile, similar
325 DSC peaks (lines 8 & 10 in **Fig. 5c**) with no detectable mass decay was noted at ~781 and ~745 °C at the Fe
326 contents of 5 and 10 *wt.*%, respectively. These conditions possibly induced secondary char formation *via*
327 repolymerization and graphitization (He et al., 2021), in agreement with the intensive carbon evolution that
328 took place at over 800 °C. In comparison, with the same amount of Fe impregnation, downward DSC peaks

329 (lines 7 & 9 in **Fig. 5b&c**) with obvious mass decays emerged at ~707 and ~747 °C, implying the
330 transformation of Fe speciation, which was also evidenced by the LCF/WT analyses (**see Supplementary**
331 **Material**).

332 Overall, in this study, these distinctions in the Fe configuration and thermal transformation suggested that
333 800 °C was a critical temperature to initiate the carbothermal reduction of crystalline Fe oxides by the labile
334 carbon. The exothermic decomposition reactions at low temperatures (illustrated as a downtrend of the DSC
335 curves in **Fig. 5c**) involved in preparation of the Fe1BC800 and Fe5BC800 resulted in deterioration of the C
336 structure in the biochar composites. Nevertheless, after forming the stable amorphous Fe compounds, the
337 impregnated Fe primarily contributed to catalytic reformation of the carbon structure at high temperatures.
338 The endothermic carbonization reactions (depicted as an uptrend of the DSC curves in **Fig. 5c**) produced the
339 Fe5BC900 and Fe10BC900 with improved graphitization and defective level. Meanwhile, the DSC curves
340 (**Fig. 5c**) corresponding to the Fe1BC900 (after a decline) and Fe10BC800 (before an ascendance) reached a
341 relatively plateau phase, which possibly offered improvement in their surface functionality and graphitization
342 level, respectively.

343

344 ***3.5 Composite reusability depends on preferable active sites***

345 The reusability of the composite is critical for determining its commercial practicability. It is noteworthy
346 that the Fe1BC900 maintained 73.2% and 64.1% of the original efficacy after 3rd and 5th use (**Fig. 6a**),

347 respectively, exhibiting the best reusability for 2,4-D adsorption. Under MW irradiation, the BC900 gave the
348 most resilient performance (*i.e.*, 67.3% of the primary capacity after 3rd use, **Fig. 6b&c**). These carbonaceous
349 materials can be regenerated through a low-temperature (at ~200 °C) thermal annealing treatment. The
350 previous research gave evidence that this process remediated 70% of the initial efficiency in a wood waste
351 biochar after 3rd run for 4-CH removal (Wan et al., 2021).

352 At ambient temperature, the FeBC composites and pristine biochars primarily consumed their graphitic
353 C−C/C=C structure after reaction with 2,4-D *via* π-π interactions (**see Supplementary Material**). Thus, the
354 intriguingly higher/lower 2,4-D adsorption by the Fe10BC800/Fe10BC900 aligned with the
355 revitalized/blocked graphitized carbon domain relative to their counterparts. In addition, the Fe1BC900
356 preferably utilized its high-level C−O/C=O groups as active sites for chemisorption (**Fig. 6d**). Meanwhile, for
357 the MW-assisted 2,4-D removal, the pristine biochars generally relied on the C−O functionality (**Fig. 6d**),
358 whereas the FeBC composites preferentially expended the C−C/C=C and C=O bonds.

359 After reaction with the Fe1BC900 or Fe5BC900 under MW conditions for three times, a negligible fraction
360 (< 0.3%) of Fe was leached or detached from the biochar composite. Their deconvoluted Raman spectra
361 demonstrated a transformation from D, G, and V_R bands to S and G_R bands, accompanied with decreased
362 values of A_D/A_G and $A_D/A_{(VR+VL+GR)}$ (**Fig. 6e and see Supplementary Material**). However, the XPS analysis
363 of C1s binding state displayed a conspicuous change from C−C/C=C to C−O/C=O bonds, and this MW-
364 triggered variation was ~3 times that under ambient condition (**Fig. 6d**). Thus, the carbon structure in the

Fe1BC900 and Fe5BC900 became more disordered and oxidized after MW reuse. Similar effects were observed with the pristine biochars (*i.e.*, BC800 and BC900). In contrast, Fe dissolution (**Fig. 6b&c**) was detected in the MW reactors when using the Fe1BC800 (1.1%), Fe5BC800 (0.4%), and Fe10BC900 (5.1%). Their carbon skeleton showed no significant changes after MW reaction compared with ambient temperature (**Fig. 6d&e**). Unlike all the other composites, after the first MW use, the Fe10BC800 presented a medium-level Fe leaching (0.6%), a more disordered carbon matrix (V_R and G bands converted into G_R and D bands, respectively), and a significant loss (17.1%) of C=O groups. Meanwhile, similar changes with the ambient condition (*i.e.*, ~20% decrease in C−C/C=C) were shown after the third use.

Accordingly, the iron and carbon phases in the FeBC composites showed different priorities for MW reaction. At the MW working frequency (*i.e.*, 2.45 GHz), owing to the prominently larger values of tan δ_E than tan δ_M for all the composites (**Fig. 2c**), the electromagnetic waves were capable of penetrating the Fe layer and directly irradiating the carbon phase. The highly graphitized and hierarchically porous carbon architecture of the Fe1BC900 and Fe5BC900, with a substantial MW absorption ability (tan δ_E = 0.548 and 0.675), which was even higher than the activated carbon (Garcia-Costa et al., 2017), would serve predominant active sites. Nevertheless, the unstable and surplus Fe particles inevitably interfered microwave propagation, which resulted in a lower MW performance of the Fe10BC900 with obvious Fe leaching. In comparison, for the crystalline Fe_3O_4 particles, a half-metallic material where electron hopping arises between the Fe^{2+} and Fe^{3+} (Shukla, 2019), might act as the chief active spots of the Fe1BC800 and Fe5BC800, because the MW

383 energy was marginally absorbed by their carbon domain and reflected to the Fe layer. Contrastingly, both the
384 carbon and Fe fractions were MW-sensitive in the Fe10BC800 deploying promoted MW capture. Its slightly
385 graphitized carbon matrix incompletely assimilated the MW irradiation, and the residual energy was taken up
386 by the Fe components.
387
388 **4. Conclusions**
389 This study demonstrates a high-efficacy, chemical-free, and energy-saving MW-assisted removal of a
390 prevalent herbicide by environmentally benign and reusable wood waste-derived MW absorbent. The design
391 of high-performance biochar lies in the science-informed customization of the pyrolytic conditions (*e.g.*, Fe
392 loading ratio and temperature). Both reductive transformation of Fe speciation and catalytic evolution of
393 carbon matrix should be simultaneously tailored and exploited during the endothermic reactions. Overall, this
394 application-oriented synthesis of the MW-reactive and environmentally friendly iron-biochar composites will
395 facilitate multifaceted improvement towards sustainable wastewater treatment as well as value-added wood
396 waste recycling.
397
398 **Supplementary Material**
399 E-supplementary data for this work can be found in the online version of the paper.
400

Acknowledgements

The authors appreciate the financial support from the Hong Kong Research Grants Council (PolyU 15222020) and Hong Kong Green Tech Fund (GTF202020153) for this study. The authors also acknowledge the equipment support provided by the University Research Facility Chemical and Environmental Analysis (UCEA) of Hong Kong Polytechnic University.

References

1. Beliy, V.A. and Udoratina, E.V., 2014. Kinetic study of wood pyrolysis in presence of metal halides. Cent Eur. J. Chem. 12, 1294-1303.
2. Cai, B., Feng, J., Peng, Q., Zhao, H., Miao, Y., Pan, H., 2020. Super-fast degradation of high concentration methyl orange over bifunctional catalyst Fe/Fe_3C@C with microwave irradiation. J. Hazard. Mater. 392, 122279.
3. Cao, M., Cai, Y., He, P., Shu, J., Cao, W., Yuan, J., 2019. 2D MXenes: electromagnetic property for microwave absorption and electromagnetic interference shielding. Chem. Eng. J. 359, 1265-1302.
4. Changela, H.G., Bridges, J.C., Gurman, S.J., 2012. Extended X-ray Absorption Fine Structure (EXAFS) in Stardust tracks: Constraining the origin of ferric iron-bearing minerals. Geochim. Cosmochim. Ac. 98, 282-294.
5. Fei, Y., Frost, D.J., Mao, H.K., Prewitt, C.T., Haeusermann, D., 1999. In situ structure determination of

the high-pressure phase of Fe_3O_4. Am. Mineral. 84, 203-206.

6. Feng, Y., Liu, P., Wang, Y., Finfrock, Y.Z., Xie, X., Su, C., Liu, N., Yang, Y.Y., Xu, Y., 2020. Distribution and speciation of iron in Fe-modified biochars and its application in removal of As(V), As(III), Cr(VI), and Hg(II): An X-ray absorption study. J. Hazard. Mater. 384, 121342.

7. Garcia-Costa, A.L., Zazo, J.A., Rodriguez, J.J., Casas, J.A., 2017. Microwave-assisted catalytic wet peroxide oxidation. Comparison of Fe catalysts supported on activated carbon and gamma—alumina. Appl. Catal. B: Environ. 218, 637-642.

8. Giannetta, B., Plaza, C., Siebecker, M.G., Aquilanti, G., Vischetti, C., Plaisier, J.R., Juanco, M., Sparks, D.L., Zaccone, C., 2020. Iron speciation in organic matter fractions isolated from soils amended with biochar and organic fertilizers. Environ. Sci. Technol. 54, 5093-5101.

9. He, M., Xu, Z., Sun, Y., Chan, P., Lui, I., Tsang, D.C.W., 2021. Critical impacts of pyrolysis conditions and activation methods on application-oriented production of wood waste-derived biochar. Bioresource Technol. 341, 125811.

10. Jette, E.R. and Foote, F., 1933. An X-Ray study of the wüstite (FeO) solid solutions. J. Chem. Phys. 1, 29-36.

11. Jing, F., Sun, Y., Liu, Y., Wan, Z., Chen, J., Tsang, D.C.W., 2022. Interactions between biochar and clay minerals in changing biochar carbon stability. Sci. Total. Environ. 809, 151124.

12. Kamali, M., Appels, L., Kwon, E.E., Aminabhavi, T.M., Dewil, R., 2021. Biochar in water and

wastewater treatment - A sustainability assessment. Chem. Eng. J. 420, 129946.

13. Karlsson, T., Persson, P., Skyllberg, U., Mörth, C.M., Giesler, R., 2008. Characterization of iron (III) in organic soils using extended X-ray absorption fine structure spectroscopy. Environ. Sci. Technol. 42, 5449-5454.

14. Kim, J.Y., Oh, S., Park, Y.K., 2020. Overview of biochar production from preservative-treated wood with detailed analysis of biochar characteristics, heavy metals behaviors, and their ecotoxicity. J. Hazard. Mater. 384, 121356.

15. Lai, F., Tian, F., Xu, B., Ye, W., Gao, Y., Chen, C., Xing, H., Wang, B., Xie, M., Hu, X., 2022. A comparative study on the degradation of phenylurea herbicides by UV/persulfate process: Kinetics, mechanisms, energy demand and toxicity evaluation associated with DBPs. Chem. Eng. J. 428, 132088.

16. Li, J., Dou, B., Zhang, H., Zhang, H., Chen, H., Xu, Y., Wu, C., 2021. Pyrolysis characteristics and non-isothermal kinetics of waste wood biomass. Energy 226, 120358.

17. Lin, H., Hong, Z., Guo, H., Yu, L., 2007. Investigation of the microwave-absorbing properties of Fe-filled carbon nanotubes. Mater. Lett. 61, 3547-3550.

18. Liu, P., Gao, S., Wang, Y., Huang, Y., Zhou, F., Liu, P., 2021a. Magnetic porous N-doped carbon composites with adjusted composition and porous microstructure for lightweight microwave absorbers. Carbon 173, 655-666.

19. Liu, Q., Zeng, M., Liu, J., Guo, B., Hao, X., Cao, Q., Shang, Y., Sun, X., Liu, J., Gao, X., 2021b. Fe-

based material@ N-doped carbon composites as environment-friendly microwave absorbers. Carbon 171, 646-657.

20. Liu, Z., Yang, X., Demeestere, K., Van Hulle, S., 2021c. Insights into a packed bubble column for removal of several ozone-persistent TrOCs by ozonation: removal kinetics, energy efficiency and elimination prediction. Sep. Purif. Technol. 275, 119170.

21. Lv, Y., Zhang, J., Asgodom, M.E., Liu, D., Xie, H., Qu, H., 2019. Study on the degradation of accumulated bisphenol S and regeneration of magnetic sludge-derived biochar upon microwave irritation in the presence of hydrogen peroxide for application in integrated process. Bioresource Technol. 293, 122072.

22. Nadejde, C., Neamtu, M., Hodoroaba, V.D., Schneider, R., Paul, A., Ababei, G., Panne, U., 2015. Green Fenton-like magnetic nanocatalysts: Synthesis, characterization and catalytic application. Appl. Catal. B: Environ. 176, 667-677.

23. Orduz, A.E., Acebal, C., Zanini, G., 2021. Activated carbon from peanut shells: 2, 4-D desorption kinetics study for application as a green material for analytical purposes. J. Environ. Chem. Eng. 9, 104601.

24. Palansooriya, K.N., Yang, Y., Tsang, Y.F., Sarkar, B., Hou, D., Cao, X., Meers, E., Rinklebe, J., Kim, K.H., Ok, Y.S., 2020. Occurrence of contaminants in drinking water sources and the potential of biochar for water quality improvement: A review. Crit. Rev. Environ. Sci. Technol. 50, 549-611.

25. Qu, J., Tian, X., Zhang, X., Yao, J., Xue, J., Li, K., Zhang, B., Wang, L., Zhang, Y., 2022. Free radicals-

triggered reductive and oxidative degradation of highly chlorinated compounds via regulation of heat-activated persulfate by low-molecular-weight organic acids. Appl. Catal. B: Environ. 310, 121359.

26. Rahmani, A., Seid-Mohammadi, A., Leili, M., Shabanloo, A., Ansari, A., Alizadeh, S., Nematollahi, D., 2021. Electrocatalytic degradation of diuron herbicide using three-dimensional carbon felt/β-PbO_2 anode as a highly porous electrode: influencing factors and degradation mechanisms. Chemosphere 276, 130141.

27. Rangabhashiyam, S. and Balasubramanian, P., 2019. The potential of lignocellulosic biomass precursors for biochar production: performance, mechanism and wastewater application-A review. Ind. Crop. Prod. 128, 405-423.

28. Shukla, V., 2019. Review of electromagnetic interference shielding materials fabricated by iron ingredients. Nanoscale Adv. 1, 1640-1671.

29. Sun, Y., Yu, I.K.M., Tsang, D.C.W., Cao, X., Lin, D., Wang, L., Graham, N.J.D., Alessi, D.S., Komárek, M., Ok, Y.S., Feng, Y., Li, X.D., 2019. Multifunctional iron-biochar composites for the removal of potentially toxic elements, inherent cations, and hetero-chloride from hydraulic fracturing wastewater. Environ. Int. 124, 521-532.

30. Sun, Y., Yu, I.K.M., Tsang, D.C.W., Fan, J., Clark, J.H., Luo, G., Zhang, S., Khan, E., Graham, N.J.D., 2020. Tailored design of graphitic biochar for high-efficiency and chemical-free microwave-assisted removal of refractory organic contaminants. Chem. Eng. J. 398, 125505.

31. Wan, Z., Sun, Y., Tsang, D.C.W., Xu, Z., Khan, E., Liu, S.D., Cao, X., 2020. Sustainable impact of tartaric acid as electron shuttle on hierarchical iron-incorporated biochar. Chem. Eng. J. 395, 125138.

32. Wan, Z., Sun, Y., Tsang, D.C.W., Yu, I.K.M., Fan, J., Clark, J.H., Zhou, Y., Cao, X., Gao, B., Ok, Y.S., 2019. A sustainable biochar catalyst synergized with copper heteroatoms and CO_2 for singlet oxygenation and electron transfer routes. Green Chem. 21, 4800-4814.

33. Wan, Z., Xu, Z., Sun, Y., He, M., Hou, D., Cao, X., Tsang, D.C.W., 2021. Critical impact of nitrogen vacancies in nonradical carbocatalysis on nitrogen-doped graphitic biochar. Environ. Sci. Technol. 55, 7004-7014.

34. Wang, H., Meng, F., Li, J., Li, T., Chen, Z., Luo, H., Zhou, Z., 2018. Carbonized design of hierarchical porous carbon/Fe_3O_4@Fe derived from loofah sponge to achieve tunable high-performance microwave absorption. ACS Sustain. Chem. Eng. 6, 11801-11810.

35. Wei, R., Wang, P., Zhang, G., Wang, N., Zheng, T., 2020. Microwave-responsive catalysts for wastewater treatment: A review. Chem. Eng. J. 382, 122781.

36. Wu, H., Gong, L., Zhang, X., He, F., Li, Z., 2021. Bifunctional porous polyethyleneimine-grafted lignin microspheres for efficient adsorption of 2, 4-dichlorophenoxyacetic acid over a wide pH range and controlled release. Chem. Eng. J. 411, 128539.

37. Wu, N., Xu, D., Wang, Z., Wang, F., Liu, J., Liu, W., Shao, Q., Liu, H., Gao, Q., Guo, Z., 2019. Achieving superior electromagnetic wave absorbers through the novel metal-organic frameworks derived magnetic porous carbon nanorods. Carbon 145, 433-444.

38. Xia, H., Li, C., Yang, G., Shi, Z., Jin, C., He, W., Xu, J., Li, G., 2022. A review of microwave-assisted advanced oxidation processes for wastewater treatment. Chemosphere 287, 131981.

39. Xu, Z., Wan, Z., Sun, Y., Cao, X., Hou, D., Alessi, D.S., Ok, Y.S., Tsang, D.C.W., 2021. Unraveling iron speciation on Fe-biochar with distinct arsenic removal mechanisms and depth distributions of As and Fe. Chem. Eng. J. 425, 131489.

40. Xu, Z., Wan, Z., Sun, Y., Gao, B., Hou, D., Cao, X., Michael, K., Ok, Y.S., Tsang, D.C.W., 2022. Electroactive Fe-biochar for redox-related remediation of arsenic and chromium: distinct redox nature with varying iron/carbon speciation. J. Hazard. Mater. 430, 128479.

41. Zeng, X., Cheng, X., Yu, R., Stucky, G.D., 2020. Electromagnetic microwave absorption theory and recent achievements in microwave absorbers. Carbon 168, 606-623.

42. Zhao, H., Cheng, Y., Lv, H., Ji, G., Du, Y., 2019. A novel hierarchically porous magnetic carbon derived from biomass for strong lightweight microwave absorption. Carbon 142, 245-253.

43. Zuanazzi, N.R., de Castilhos Ghisi, N., Oliveira, E.C., 2020. Analysis of global trends and gaps for studies about 2, 4-D herbicide toxicity: A scientometric review. Chemosphere 241, 125016.

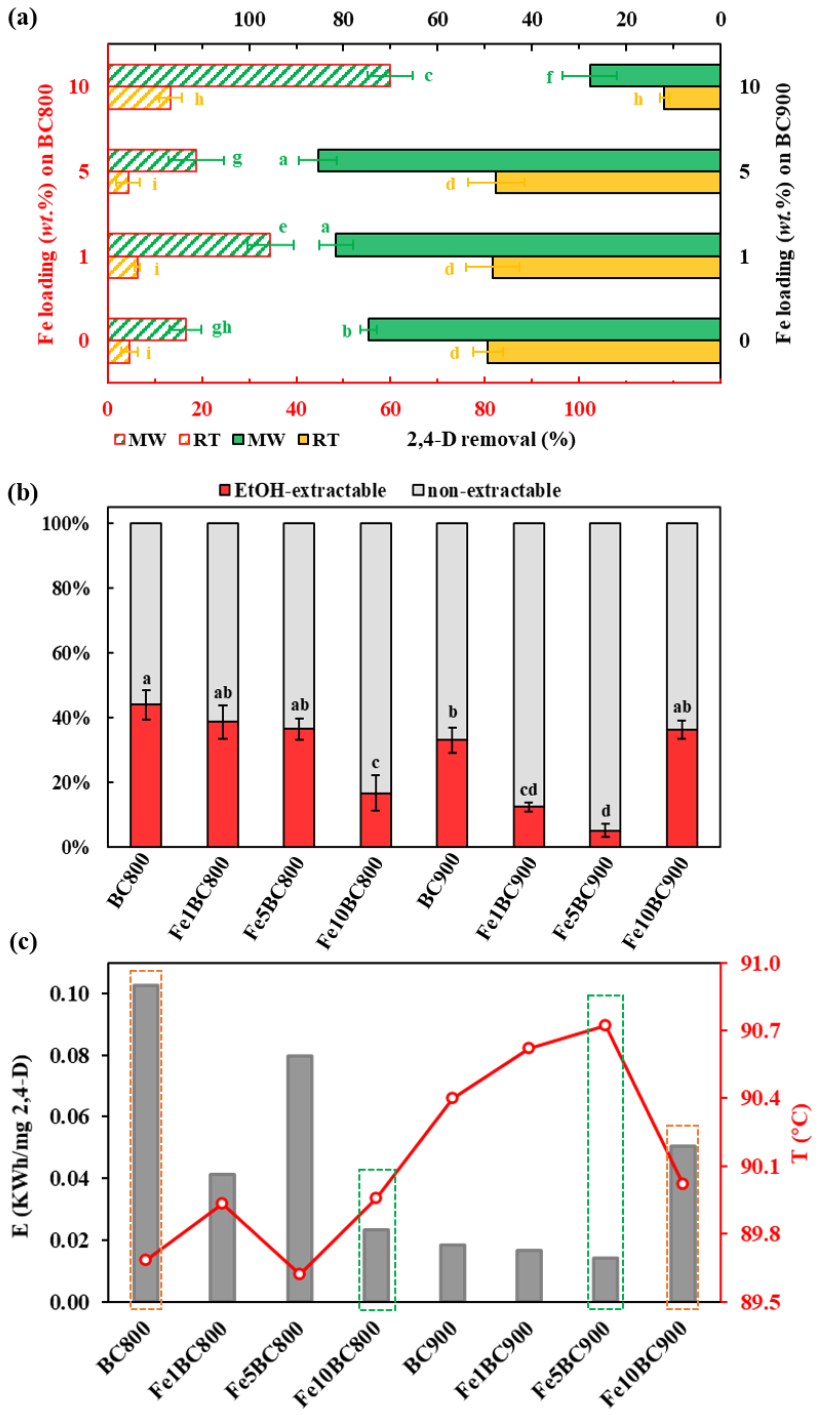

Fig. 1. Comparison of 2,4-D removal performance under room temperature (RT) and microwave (MW) conditions (a); 2,4-D affinity (based on the ethanol (EtOH) extractability after reaction) under MW condition (b); and MW energy efficiency (according to the electricity consumption and reactor temperature during 2,4-D removal) (c) of the FeBC composites (lower-case letters indicate the significance levels ($p < 0.05$) of differences).

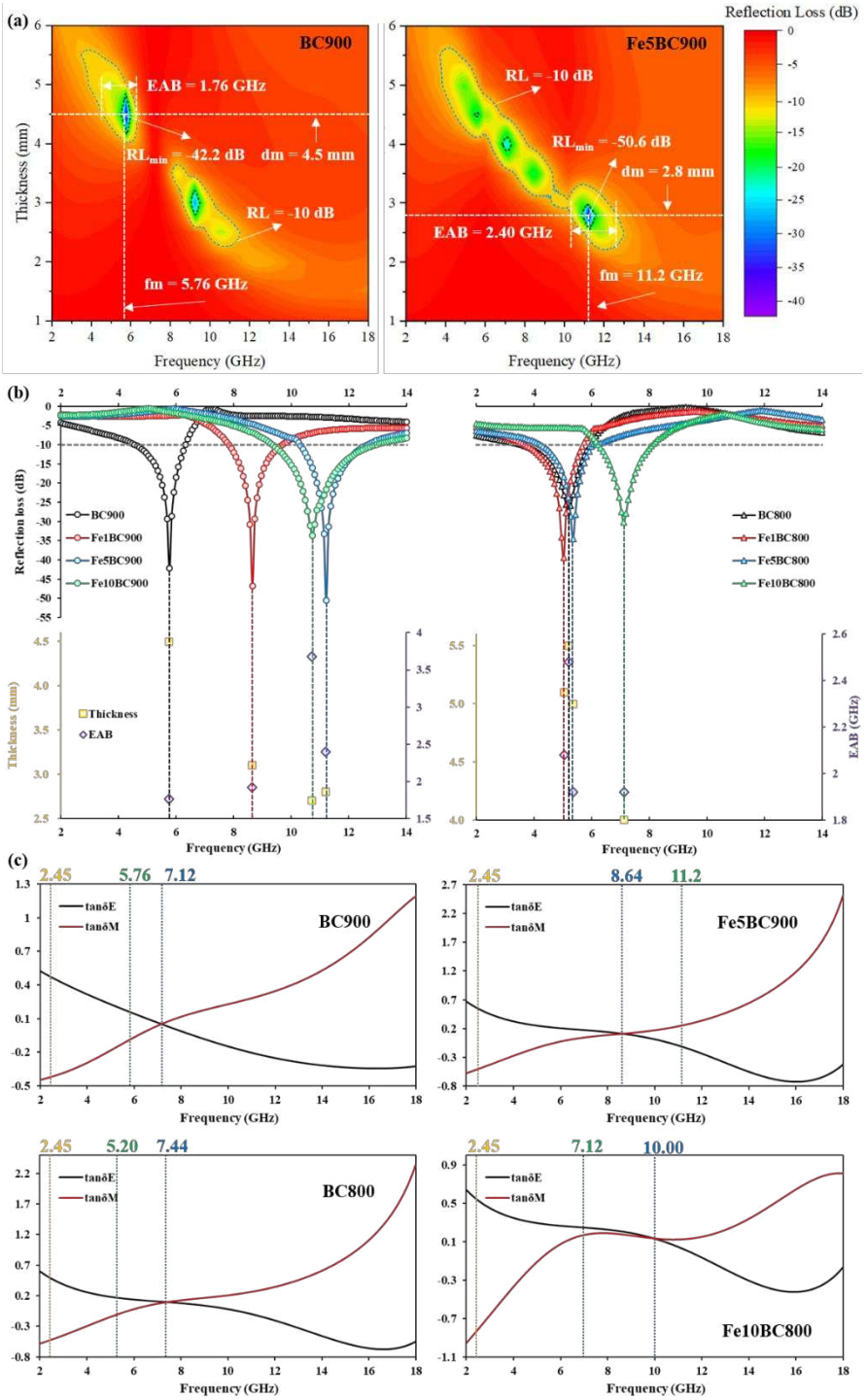

Fig. 2. Comparison of microwave (MW) absorption ability of the FeBC composites with frequency (2−18 GHz): (a) 2D projection of reflection loss (RL) values (RL = -10 dB, 90% MW absorption); (b) minimum reflection loss (RL_{min}) values with corresponding frequency (f_m), composite thickness (d_m), and effective absorption bandwidth (EAB); and (c) tangent magnetic loss ($tan\delta_M$) and dielectric loss ($tan\delta_E$) values (yellow line: working frequency of the MW reactor; green line: f_m).

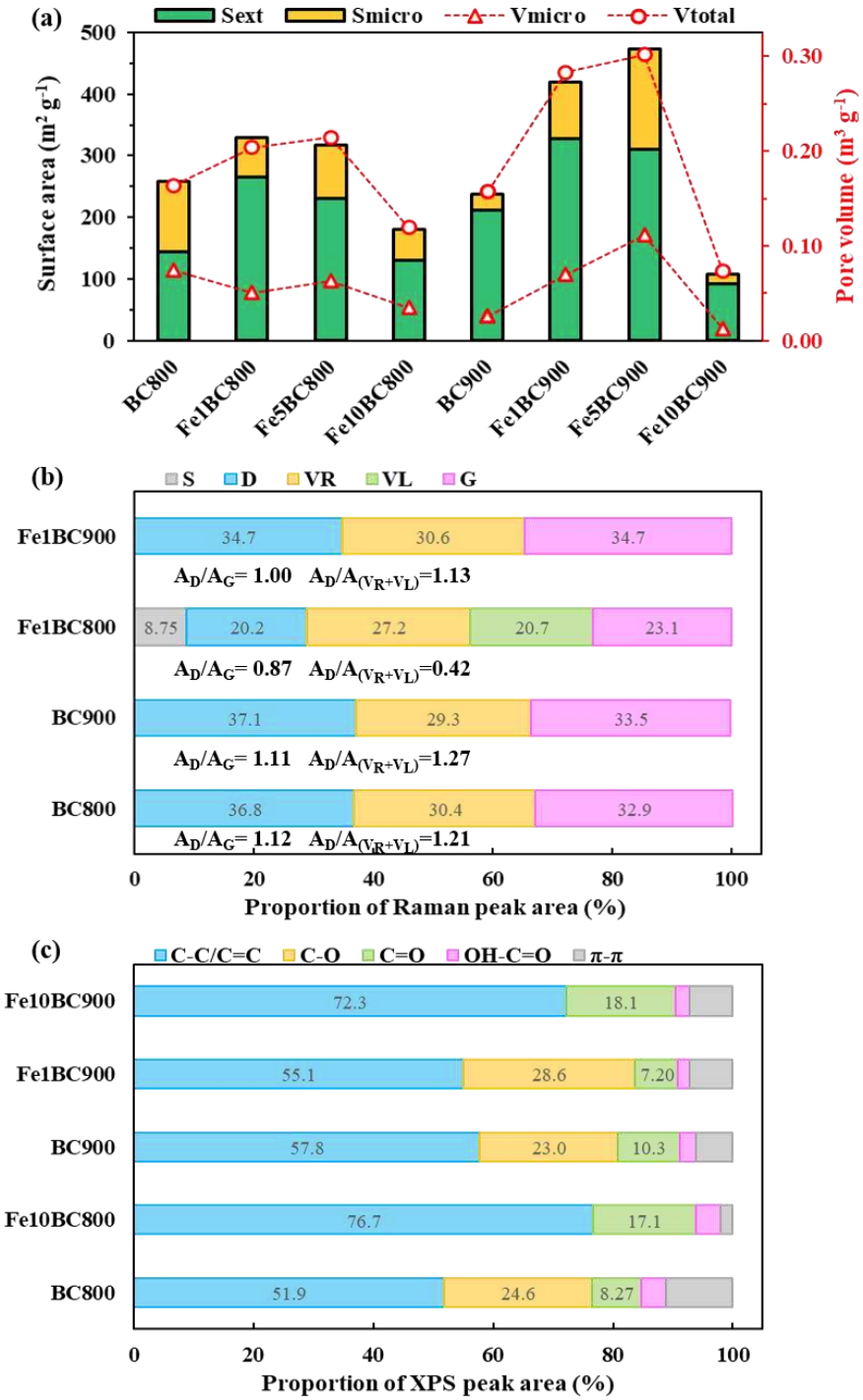

Fig. 3. Surface area and porosity (a); Raman analyses (b); and XPS results (c) for the selected FeBC composites.

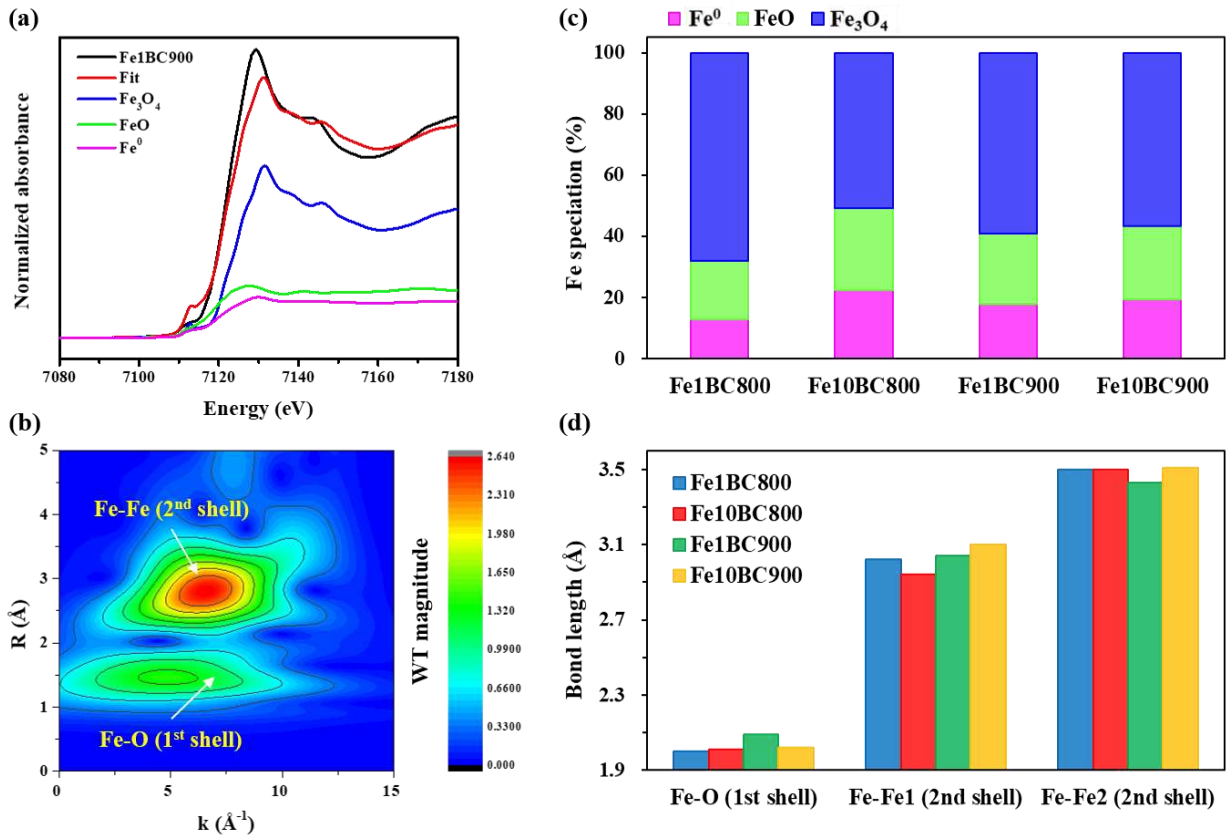

Fig. 4. Edge-step normalized Fe *K*-edge XAFS spectra (a) and high-resolution WT plot displaying the first and second coordination shells (b) of the Fe1BC900. Fe speciation (c) calculated from XANES-LCF and bond length (d) modelled from EXAFS analyses of the selected FeBC composites.

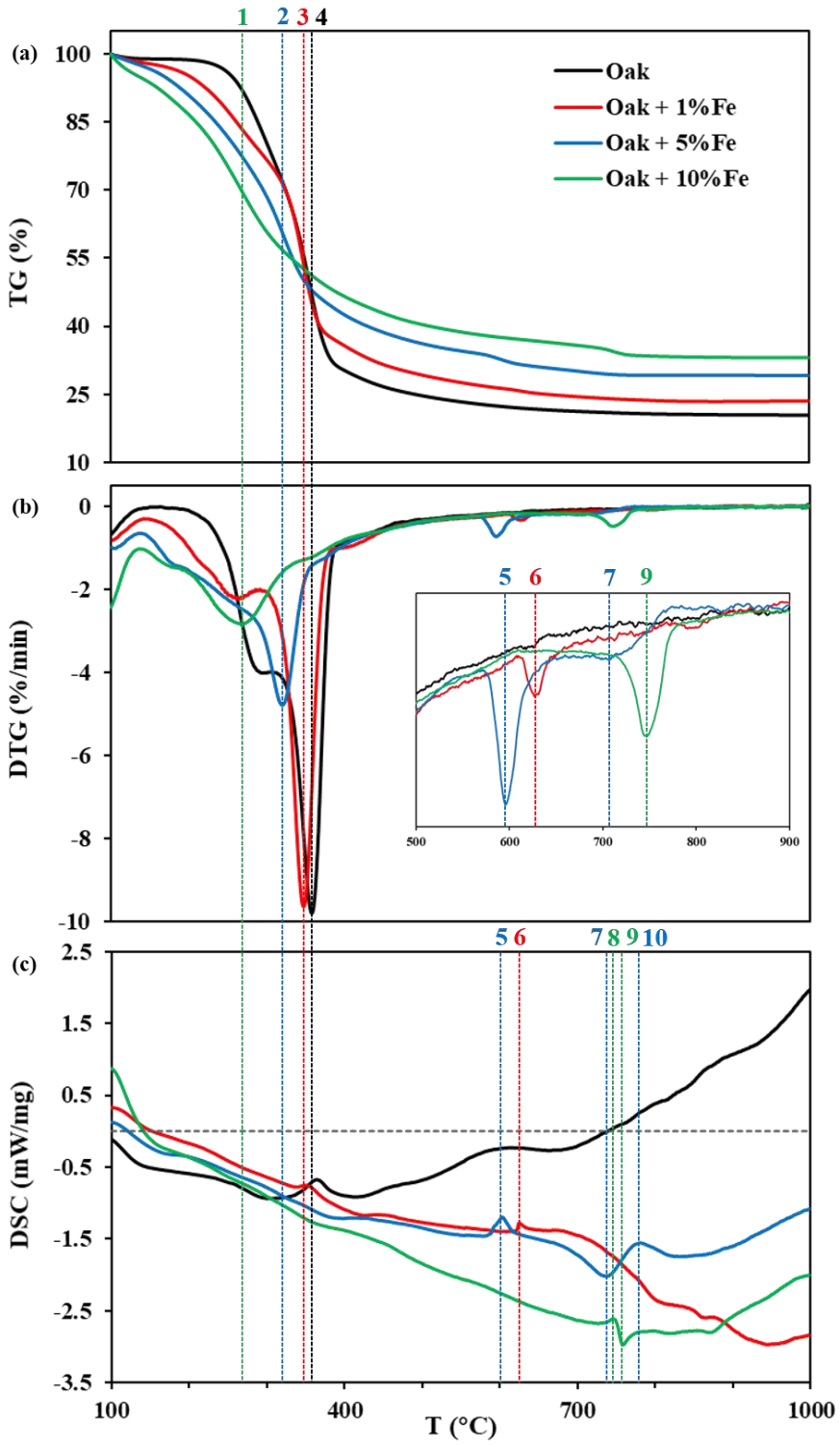

Fig. 5. TG (a); DTG (b); and DSC (c) analyses of the Fe-oak mixtures (1−4: char formation; 5 & 6: char cracking; 7 & 9: transformation of Fe speciation; 8 & 10: secondary char formation).

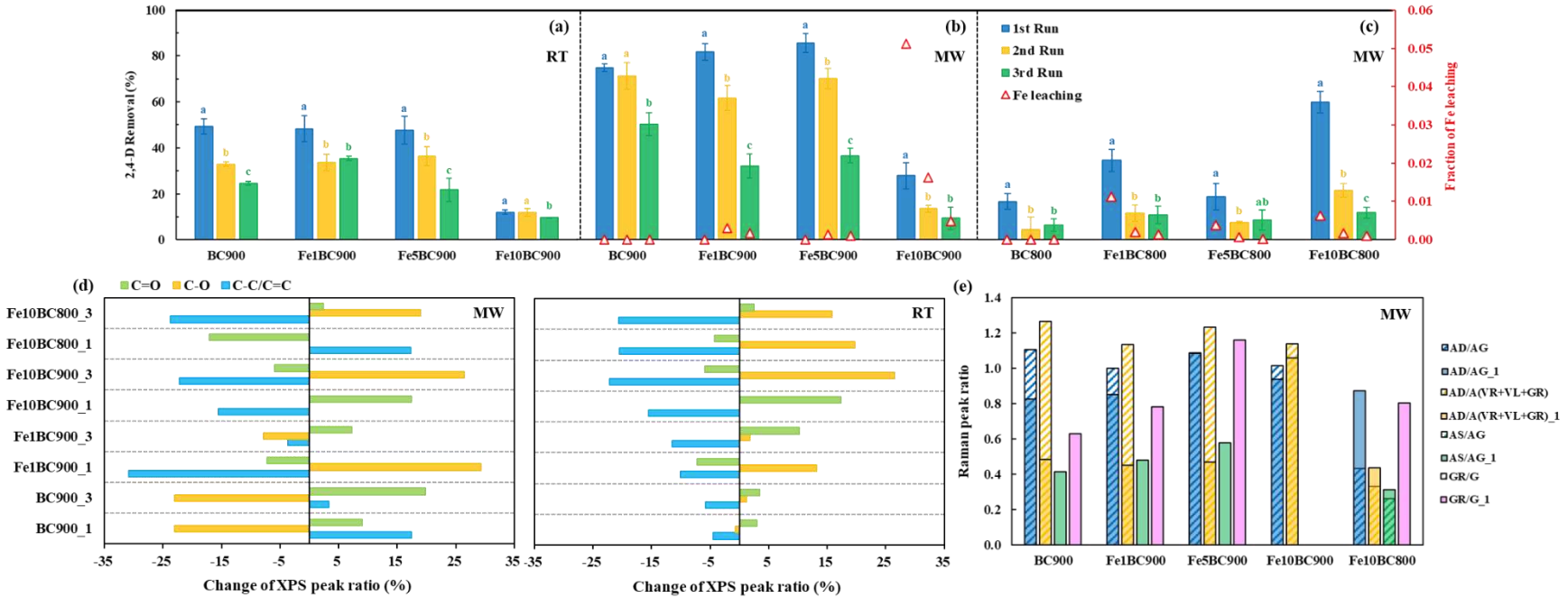

Fig. 6. Reusability of the FeBC composites under room temperature (RT) (a) and microwave (MW) (b&c) conditions. Characterization of the FeBC composites after reuse by XPS C1s (d) and Raman (e) analyses (1: after 1st use; 3: after 3rd use; the change of XPS peak ratio was relative to the previously used composite).